

Fig. 2. Derivative process of high saliency ratio rotor.

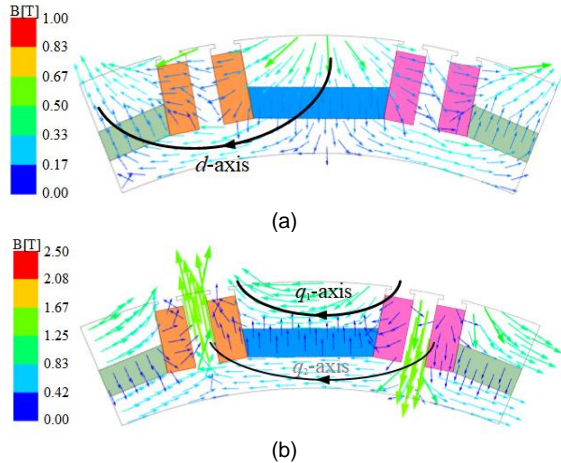


Fig. 3. Path of d - and q -axis. (a) d -axis. (b) q -axis.

rotor are employed which have the same PMs volume. Furthermore, the 16-pole 72-slot structure is selected to reduce the torque ripple and ensure the high saliency ratio of the motor, while retaining reluctance torque capability. With optimized PM shape and position, the motors are established. Additionally, the back electromotive force (EMF), air-gap flux density, cogging torque, saliency ratio, maximum torque per ampere (MTPA) capability, field-weakening capability, loss and efficiency of the machines are analyzed and compared. Finally, the experiment of electromagnetic performance is tested to verify the results of the finite element analysis (FEA).

II. TOPOLOGIES AND FEATURES

A. Machine topology

Derivative process of the motor with the proposed rotor is shown in Fig. 2.

A spoke-type IPM motor (named M1) generates flux leakage at the inner circumference of the rotor due to its flux-concentrating rotor structure, and therefore degrades the motor performance. But Halbach PM array (named M2) with the unilateral magnetic shielding is an effective method to reduce

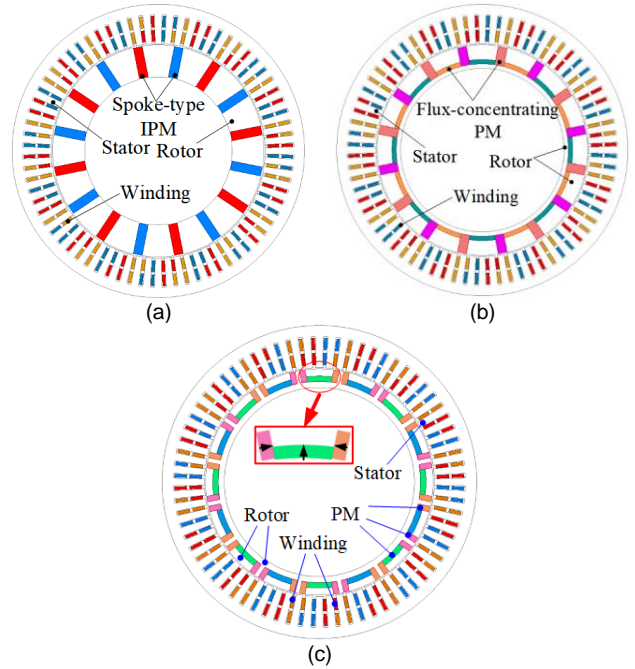


Fig. 4. IPM machines with different rotors. (a) Spoke-type motor (M1). (b) The new flux-concentrating motor (M2). (c) The high saliency ratio motor (M3).

the flux leakage. Then the new flux-concentrating is proposed (named M3). For this structure, the upper part is the same as spoke-type IPM motor which PMs are magnetized tangentially, which can achieve the purpose of flux concentration, and the bottom part is Halbach PM array that can reduce flux leakage at the inner circumference of the rotor. In [28], the performance of a motor with this rotor is described in detail. For vehicles, reliability and acceleration performance at high speed are important indicators to measure the dynamics. Therefore, the motor on board needs high power density and wide CPSR. In order to further utilize the reluctance torque, tangentially magnetized PMs are divided into separate parts to reduce the reluctance of the q -axis path. The new spoke-type IPM machine with enhanced flux-concentrating capability and high saliency ratio rotor (M3) is proposed. This structure retains the flux concentration characteristic of the spoke-type IPM motor, while the Halbach PM array suppresses the flux leakage at the inner circumference of the rotor. Furthermore, the saliency ratio increases further and the potential reluctance torque can be more utilized.

Fig. 3 is a diagram of the d - and q -axis paths of the proposed rotor. The resistance of the PMs is much greater than that of the rotor core. The relative permeability of the rotor core is assumed to be infinite. It can be seen that the resistance of the d -axis includes the reluctance of rotor core and radially magnetized PMs, while the magnetic resistance of the q -axis is much smaller. For this rotor structure, when the current angle control is applied appropriately, the proposed model can utilize both magnetic torque and reluctance torque because of the high saliency ratio. The innovation of this structure is the path of q_2 -axis. L_q is larger than before and the saliency ratio is increased ($\rho = L_q / L_d$). This paper will analyze the electromagnetic performance of this model and a motor with spoke-type rotor in Section-IV.

TABLE I
MACHINE SPECIFICATION

Design parameters	M1	M2	M3
Poles and slots		16-72	
Continuous phase current/ A_{rms}		100	
Maximum phase current/ A_{rms}		300	
Continuous rated power/ kW		60	
Rated speed/ $r \min^{-1}$		3000	
Outer diameter of stator/mm		260	
Inner diameter of stator/mm		190	
Outer diameter of rotor/mm		188	
Inner diameter of rotor/mm	133	146	177
Winding factor		0.945	
Stack length/mm		75	
Air-gap length/mm		1	
PM material		SmCo, $B_r = 1.1 \text{ T}$, $H_c = -826 \text{ kA/m}$	
PM weight/kg		1.99	
Core material		B20AT1500	
Inverter		$f_c = 10 \text{ kHz}$, $V_{DC} = 420 \text{ V}$	

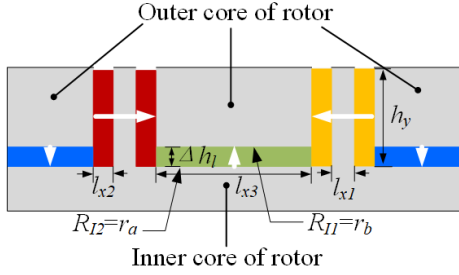


Fig. 5. Design variables in the optimized topologies.

TABLE II
INITIAL VALUE AND VARIATION RANGE OF DESIGN VARIABLES

Variables	Initial value/mm	Range
l_{x1}	4	4~6
l_{x2}	3	2.5~4.5
l_{x3}	17	16~20
h_y	8	7~10
Δh_l	3	3~5
Δh_l	4	3~6
r_{as}	77	>77

B. Machine specifications

This machine is designed for EREVs. Fig. 4 schematically shows three magnet configurations. The total mass of the PMs in the rotors are identical, so the material cost is consistent. For one polar, three pieces of magnets make up the proposed rotor (named M3), the spoke-type rotor (named M1) has one piece of magnet and the new flux-concentrating rotor (named M2) has two pieces of magnets. The specification of the three IPM machines is listed in Table I, the stators are identical, and fluid cooled is adopted by the machines. The continuous phase current is 100 A_{rms} , the maximum phase current is 300 A_{rms} .

III. ROTOR OPTIMIZATION

Considering the influence of the stator structure on the d -axis inductance, the stack length, outer and inner diameter of the stators are determined (in Table I). Because the motor is connected to the vehicle chassis system, the ambient

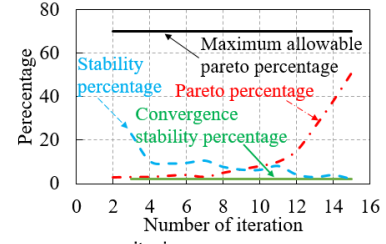


Fig. 6. Convergence criteria.

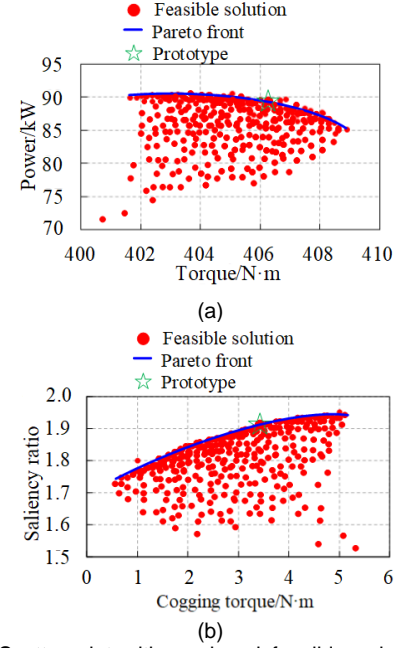


Fig. 7. Scatter plot with produced feasible solutions in the optimization (M3). (a) Torque VS power. (b) Saliency ratio VS cogging torque.

temperature is high. Compared with NdFeB, the advantage of high temperature resistance for SmCo is obvious. And SmCo is selected for this model.

In order to illustrate the superiority of the proposed rotor, the three rotors are optimized with the identical stator. The variables of the topologies are shown in Fig. 5. l_{x1} is the distance between the two adjacent PMs of neighboring poles, l_{x2} is the width of the vertical PMs, l_{x3} is the width of the horizontal PMs, h_y is the height of the vertical PMs, Δh_l is the height of the horizontal PMs. When neglecting the influence of stator resistance, the voltage of a PMSM can be expressed as:

$$u = \omega_r \sqrt{(L_q i_q)^2 + (L_d i_d + \psi_f)^2} \quad (1)$$

where ω_r , L_d , L_q , i_d , i_q and ψ_f are the rated speed, d - and q -axis inductances, d - and q -axis current and PM flux, respectively.

When u is fixed as 420 V, the increase in the saliency ratio ρ results in a decrease of the rated speed ω_r according to (1), which can influence the peak power of the motors. When designing a PM motor, many different of design objectives are set, according to applications. However, in this paper, a typical set of EREVs traction motor design includes power, cogging torque and wide-speed operation. Taking into account the errors of the model and experiments, the optimization objectives are saliency ratio ($\rho > 1.8$), torque ($T > 400 \text{ N m}$), power ($P > 85 \text{ kW}$) and cogging torque ($T_{cog} < 4 \text{ N m}$). Meanwhile, efficiency

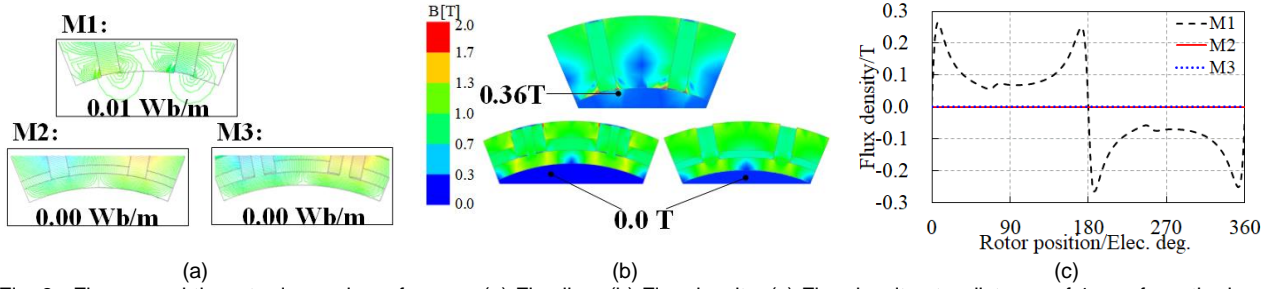


Fig. 8. Flux around the rotor inner circumference. (a) Flux line. (b) Flux density. (c) Flux density at a distance of 1 mm from the inner circumference of the rotor.

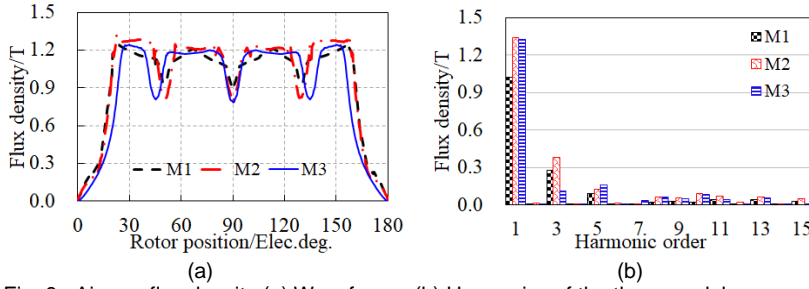


Fig. 9. Air-gap flux density (a) Waveforms. (b) Harmonics of the three models.

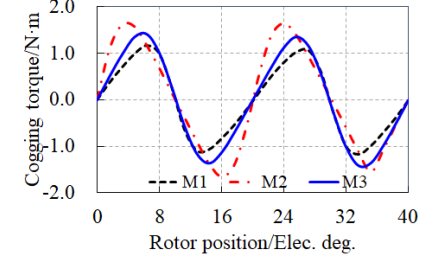


Fig. 10. Cogging torque of the three models.

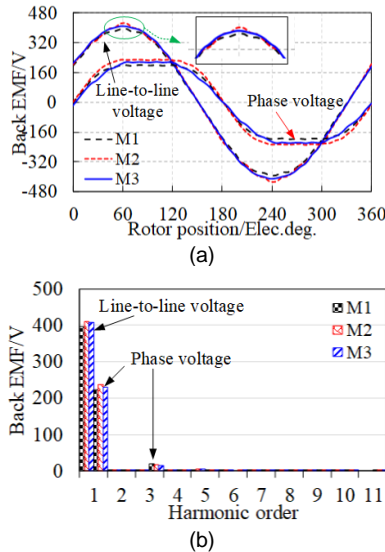


Fig. 11. Back-EMFs of the three models. (a) Waveforms. (b) Harmonics of line-to-line voltage and phase voltage.

is improved by optimizing torque and power, indirectly. The values of the key design variables of the high saliency ratio rotors are listed in Table II.

In this paper, the effective method multi-objective genetic algorithm (MOGA) is applied to conduct the multi-objective optimization of the proposed rotor [29], [30]. When optimization is in progress, different conditions are set, 100 is the initial samples number, the probability of crossover is set to 0.9, 50 is the number of samples per iteration, and 0.05 is assigned to the probability of mutation. In addition, how to judge whether the optimization process is complete, there are three kinds of conditions are set for this. Namely, maximum iterations which number is set to 16. The population of each generation is 50. The value of the maximum allowable Pareto percentage is set to 70, and 0.2 is assigned to the convergence stability percentage. When any one of the three convergence

criteria reach the set number, the optimization will stop, as shown in Fig. 6.

The Pareto front of the feasible solutions are illustrated in Fig. 7. By comparing the amounts of PMs with these points that meet the optimization goals at the same time, the final result is: $l_{x1}=3.75$ mm, $l_{x2}=4.6$ mm, $\Delta h_f=4.5$ mm, $h_y=10.5$ mm, $l_{x3}=20.5$ mm, $r_a=83.5$ mm, $r_b=88$ mm. The PM mass is 1.99 kg.

IV. FEA VERIFICATION

In order to verify the superiority of the proposed model, ANSYS Maxwell software is employed to do FEA. Additionally, for fully and fairly comparing the performance of the three motors, the simulation software and excitation are the same.

A. Open-circuit characteristics

The no-load characteristics mainly include air-gap flux density, back-EMF and cogging torque.

Fig. 8 (a) and Fig. 8 (b) shows the flux leakage distribution around the inner circumference of the rotor. Fig. 8 (c) describes the flux leakage at a distance of 1 mm from the inner circumference of the rotor. It can be seen that the flux leakage of M2 and M3 is close to 0 T, while the amplitude in M1 is above 0.08 T. The air-gap flux density affects the performance of the motor. Fig. 9 (a) plots the waveforms of the air-gap flux density in one pair of poles. With the flux-concentrating capability, the air-gap flux density amplitude of M2 and M3 is higher than that of the M1. As shown in Fig. 9 (b), the fundamental amplitudes of the air-gap flux density are 1.02, 1.34 and 1.33 T. The 5th, 7th harmonics in M3 is a little higher than that in M1 [31]. The total harmonic distortion (THD) percentage of the three models is 29.44%, 32.42% and 19.00%. The 5th and 7th harmonics increased by 26.3% and 33.1%, respectively. The order of the air-gap flux density harmonics that generate cogging torque are 5th, 7th, 11th and 13rd [32]. The cogging torque is shown in Fig. 10. The peak-to-peak value of the cogging torque increases from 2.28 N·m in M1 to 3.68

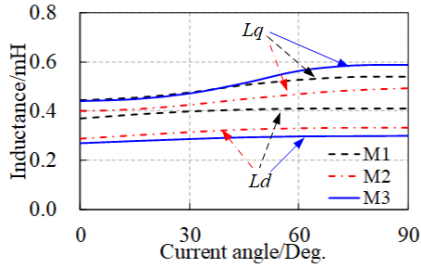


Fig. 12. Calculated L_d and L_q versus current angle (100 A_{rms} of phase current).

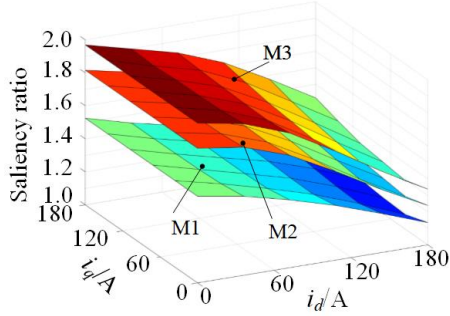


Fig. 13. Saliency ratio.

TABLE III
COMPARISON OF SALIENCY RATIO FOR COMMERCIAL OR PUBLIC MOTORS

Conditions	Rated condition	Peak power	Maximum speed
M3	1.908	1.317	2.106 (at 6000 r/min)
The motor of Tesla Model 3 (V-type)	1.992	1.227	3.081 (at 12000 r/min)
The motor of Prius 2004 (V-type)	1.772	1.128	1.986 (at 6000 r/min)
Reference [26]	1.650	—	—
Reference [27]	1.380	—	—

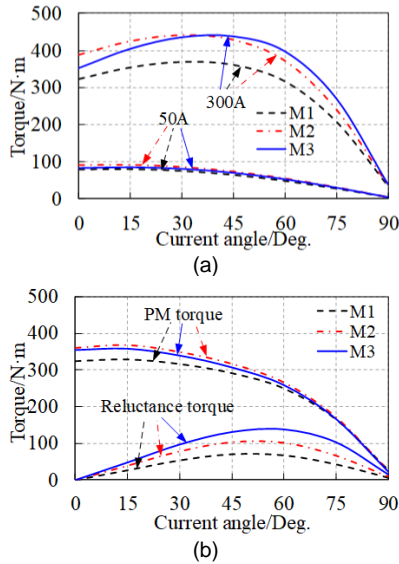


Fig. 14. Torque characteristics. (a) Output torque versus current and current angle. (b) Torque separation at 300 A_{rms} of phase current, 3000 r/min.

N·m in M3, about 40.24%. The air-gap flux density is different in the three models because of the rotor structure. The air-gap flux density of M3 is larger than that of M1, so the cogging

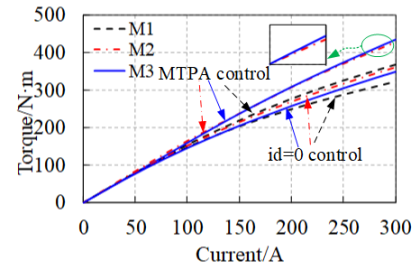


Fig. 15. Calculated MTPA and $i_d=0$ capability.

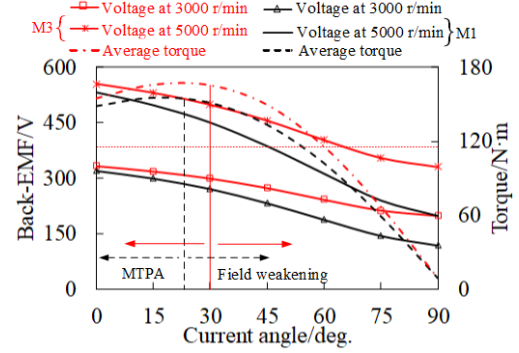


Fig. 16. Calculated field-weakening capability.

torque is also large. However, it only accounts for 0.92% of the average torque in M3 which has a negligible effect on the dynamic performance of the machine.

Although the cogging torque affects the low-speed performance of the motor and has a negative effect on high-precision positioning in a position control system, it accounts for a very small proportion of the electromagnetic torque.

Fig. 11 (a) is the simulated back-EMFs of the three models, and their harmonics are shown in Fig. 11 (b). The amplitude of back-EMFs in the three models are 397, 411.2 and 408 V of line-to-line voltage, and 223, 237.4 and 230 V of phase voltage, respectively. It can be seen that only a few 3rd harmonics are present in the phase back-EMFs, and little harmonics exist in the line-to-line back-EMFs.

B. Saliency ratio

Fig. 12 plotted the calculated L_d and L_q at the rated current with respect to the current angle. Fig. 13 compares the saliency ratio of the three models with different value of i_d and i_q at 3000 r/min. It is obvious that the saliency ratio of M3 is the highest in the three models, which will result in a potential torque improvement, especially reluctance torque. The principle of high saliency ratio is introduced in Section III – A. By reducing the magnetic resistance of q -axis, L_q is large and the saliency ratio increases. When the saliency ratio is large, high reluctance torque is conducive to increase the output torque. This can be seen in (2):

$$T_e = \frac{3}{2} p (\Psi_f i_q - \Psi_q i_d) = \frac{3}{2} p \Psi_f i_q + \frac{3}{2} p (L_d - L_q) i_d i_q \quad (2)$$

where p is number of pole pairs, Ψ_f is magnetic flux, i_d , i_q , L_d and L_q are the current of d -axis and q -axis, inductance of d -axis and q -axis, respectively. The former is electromagnetic torque and the latter is reluctance torque.

Additionally, Table III compares the saliency ratio of two

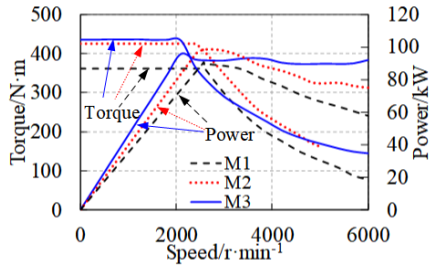


Fig. 17. Torque and power (under 300 A_{rms} of phase current and 420 V DC-bus voltage).

TABLE IV
LOSSES OF THE TWO MODELS BY FEA

Rated condition	1000		3000		4000	
	M2	M3	M2	M3	M2	M3
Copper loss/kW	0.90	0.90	0.90	0.90	0.90	0.90
Iron loss/kW	0.10	0.08	0.359	0.294	0.457	0.377
PM loss/kW	0.013	0.007	0.029	0.008	0.040	0.027
Total loss/kW	1.013	0.987	1.288	1.202	1.397	1.304
Torque/N·m	139.5	128.0	140.1	128.0	65.2	66.7
Torque ripple (peak-to-peak value)/%	7.88	4.81	7.86	4.90	9.45	7.69
Power/kW	14.6	13.4	44.0	40.2	27.3	27.9
Efficiency/%	93.0	92.2	97.1	97.0	94.9	95.3

The winding excitation is sinusoidal wave current.

commercial EV motors (Tesla Model 3 and Toyota Prius 2004) and two published IPMs. Under the peak power conditions, saliency ratio of the proposed prototype is the highest, up to 1.317. The maximum speed of the proposed prototype is 6000 r/min, which is 12000 r/min in Tesla Model 3. In the future, a motor with the proposed rotor will be developed for EVs and the maximum speed of traction system is expected to be 24000 r/min. The saliency ratio at the maximum speed conditions will be updated.

C. Torque performance and MTPA capability

Fig. 14 (a) is the waveforms of output torques with respect to the current angle under different currents. It can be seen that, in the three models, the variation of the average torque with respect to the current angle and the maximum torque per ampere (MTPA) angles ranges from 30 to 45 electrical degrees. As the current angle increases, the output torque decreases, when the angle is beyond this range. The torque separation of the three models under the phase current of 300 A_{rms} , 3000 r/min by the frozen permeability method is shown in Fig. 14 (b). The PM torque of M3 is higher than that of M1 but lower than that of M2 due to the flux density. However, the reluctance torque is different. The reluctance torque of M3 is the largest. It indicates that the current angle can be controlled. By changing the current angle the reluctance torque production is achievable. When the reluctance torque is more fully utilized, the electromagnetic torque of M3 is higher than that of M2.

Fig. 15 also compares the MTPA capability of the three motors, numerically. Meanwhile, the $i_d = 0$ control capability is also plotted. The results show that MTPA control can output higher torque in these models. Additionally, when the current is

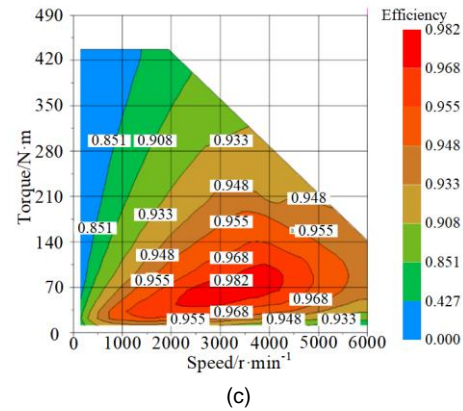
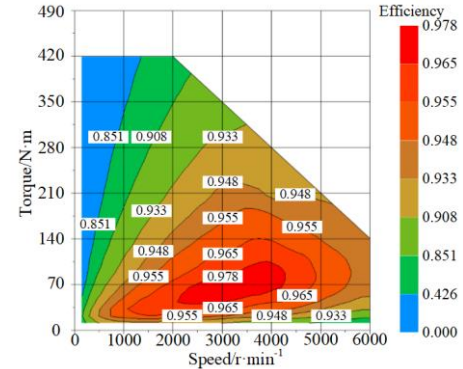
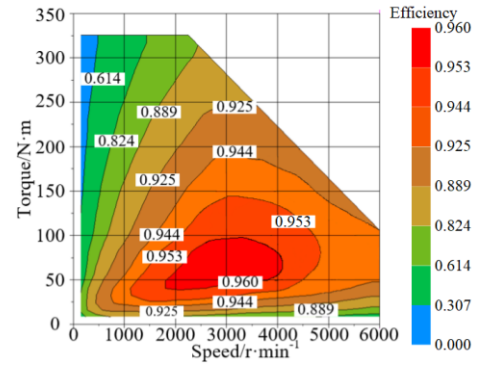


Fig. 18. Efficiency map of three models. (a) Efficiency of M1. (b) Efficiency of M2. (c) Efficiency of M3.

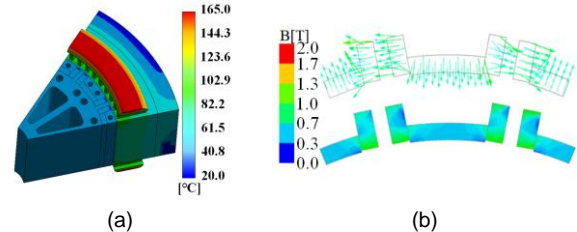


Fig. 19. Temperature and flux density. (a) The temperatures distribution under the phase current of 300 A_{rms} , at 90 kW. (b) The flux density of PMs is 0.9 T.

low or $i_d = 0$ control is adopted, the PM torque has a great influence on the output torque, so the electromagnetic torque of M2 is higher than that of M3. However, by utilizing the reluctance torque, when the MTPA is active, the torque of M3 is higher than that of M2, especially when the current is larger. In any case, M1 has the lowest torque.

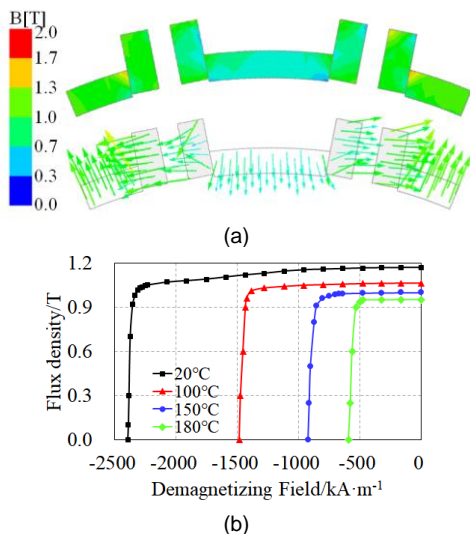


Fig. 20. Flux density of PMs under extreme conditions. (a) The flux density of PMs is 0.96 T. (b) Demagnetization characteristic curves of SmCo.

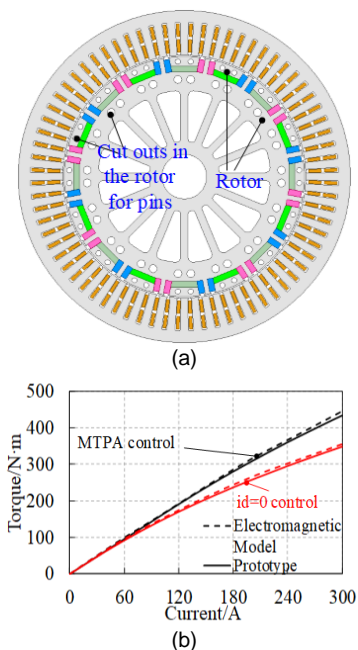


Fig. 21. Model of prototype. (a) Model. (b) Torque versus current.

D. Field-weakening capability

Due to the DC link voltage limit, when $i_d=0$ control is adopted, that is, when the current angle is 0, for the speed, there is a limit value. For EVs, the operating conditions are complex, field-weakening control is required to expand the operating speed range. Taking the control voltage margin into account, the phase voltage is limited to 171.5 V_{rms} or even less in the three motors. M1 and M3 are used as examples.

Under the voltage conditions, Fig. 16 shows an exemplary graph which gives the output torque at 100 A_{rms} of phase current and the corresponding back-EMF voltage at 3000 r/min and 5000 r/min. It can be seen that below 30 electrical degrees, the MTPA control is effective in M3, whereas this angle is 15 degrees in M1. When beyond that angle, the field-weakening

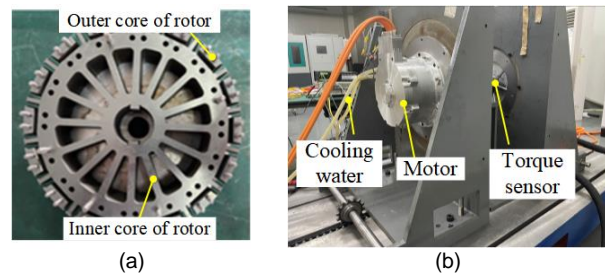


Fig. 22. Prototype motor. (a) Rotor assembly. (b) Test platform.

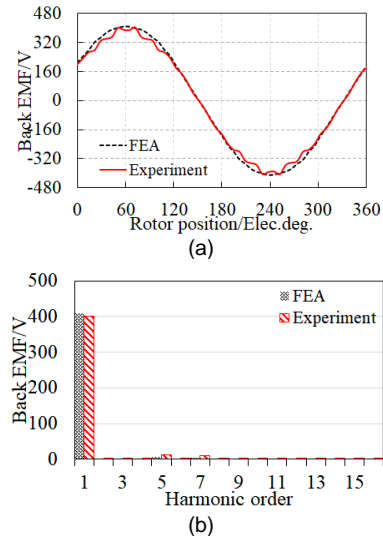


Fig. 23. Back-EMF. (a) Measured and FEA no-load line-to-line back-EMF voltage (at 3000 r/min). (b) Harmonics.

control needs to be applied because of the voltage limit. For example, the current angle is around 30 electrical degree, if the motor operates at 3000 r/min. The output torque is about 165 N·m. But when the motor runs at 5000 r/min, the estimated current angle is around 70 electrical degrees and the output torque is about 88 N·m. In M3, the voltage decreases more slowly. According to (1), (3) and Fig. 12, the rated speed decreases and the maximum speed increased. The field-weakening area becomes large.

$$n = \frac{60 \times u_{lim}}{2\pi p |\varphi_f - L_d i_{lim}|} \quad (3)$$

where p is number of pole pairs, φ_f is magnetic flux, L_d is inductance of d -axis, u_{lim} and i_{lim} are the voltage limit and current limit, respectively.

E. Loss and efficiency

Fig. 17 shows the torque and power characteristics at the maximum 300 A_{rms} of phase current, DC link voltage of 420 V. And a wide constant power region of 90 kW can be achievable from 2000 to 6000 r/min. The peak power of three model is 89.1, 98.5 and 92.7 kW. Only M3 maintains constant power when operate at 2000 to 6000 r/min. To show the composition of losses at different speed clearly, the FEA are employed to segregate them, as listed in Table IV. The excitation is sinusoidal wave current. Phase current is 100 A_{rms} and DC-bus voltage is 420 V. At the same phase current and different speed, it can be seen that the efficiency of M3 is a little lower than that

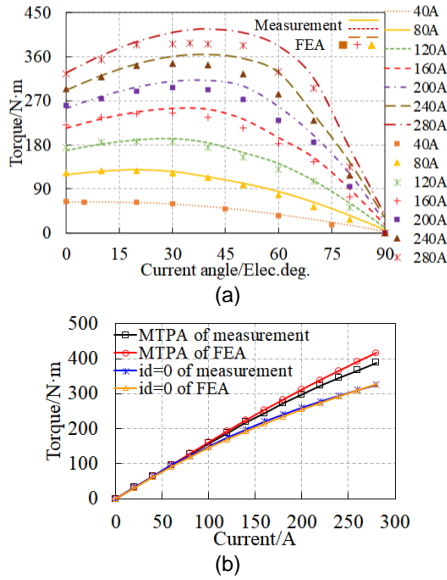


Fig. 24. Torque characteristics. (a) Output torque versus phase current and current angle (at 100 r/min). (b) MTPA and $i_d=0$ capability.

of M2, when the speed is low. But when the speed is high, the torque/power of M3 is higher than that of M2. Furthermore, the efficiency of M3 is high.

The efficiency map of FEA is shown in Fig. 18, including friction loss, under the given DC link voltage of 420 V and 300 A_{rms} of phase current. This efficiency map covers the entire operable points of the motor. The loss is obtained by sinusoidal pulse width modulation current excitation. Under the same operating conditions, the efficiency in the efficiency map is different from that in Table IV because the excitation is different, one is sinusoidal wave current and the other is sinusoidal pulse width modulation current. The distribution of efficiency is similar for M2 and M3. It can be seen that the maximum efficiency reaches up to 98.2% when the motor is driven near 70 N·m, 3000 r/min in M3, which is 2.20% and 0.40% higher than M1 and M2, respectively. However, the 96% region is limited to less than the speed of 4000 r/min for M1 because of the increased iron loss and PM loss in high speed.

F. Demagnetization analysis

The temperature rise will bring the risk of irreversible demagnetization of PMs. Fig. 19 (a) shows the temperature field results for phase currents of 300 A_{rms} at 3000 r/min. The corresponding power is 90 kW. The temperatures of PMs are 78.3°C. The flux density and the magnetization direction of the PMs are shown in Fig. 19 (b). When the motor works at 6000 r/min and the three-phase winding is short-circuited suddenly, the risk of irreversible demagnetization of the PMs is the greatest. The instantaneous current amplitude is about 300 A. Fig. 20 (a) plotted the flux density at the extreme conditions. According to the demagnetization characteristic curves of SmCo, there is a low risk of demagnetization when the PMs flux density is 0.9 T and 0.96 T, respectively.

V. EXPERIMENTAL VERIFICATION

This section introduces the performance evaluation and experimental verification the of the 72-slot /16-pole prototype.

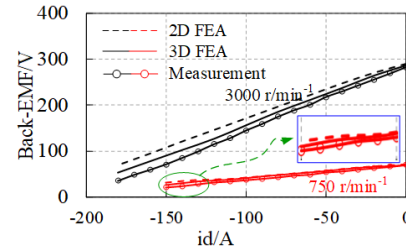


Fig. 25. Field-Weakening capability.

TABLE V
SPECIFICATIONS OF THE VEHICLE

Parameters	Value
Mass	1144 kg
Drag coefficient	0.335 cd
Front Area	2 m ²
Coefficient of aerodynamic resistance	0.34
Rolling resistance coefficient	0.015

There are some adjustments done in order to ensure the structural integrity of the rotor prototype. The prototype model of FEA is shown in Fig. 21 (a). The rotor consists of two parts, called the rotor inner core and the rotor outer core. Some cut outs in the rotor which decreased the electromagnetic properties of M3. Torque drops from 440 to 434 N·m. Fig. 21 (b) compares the output torque. Fig. 22 plots the prototype.

The no-load line-to-line back-EMF waveform at 3000 r/min is shown in Fig. 23 (a), and the measured value turned out to be 282.27 V_{rms} which is 4.95% lower than the experimental value. This error is acceptable.

Fig. 23 (b) compares the harmonics of the FEA and experimental back-EMFs. The THD of FEA result is 2.29%. It is 4.53% in experimental result.

In order to reduce the effects related to speed, the output torque versus phase current and current angle is measured at 100 r/min. The results are shown in Fig. 24 (a). The MTPA capability is plotted in Fig. 24 (b). When the phase current is small, there is a good agreement between the analysis and the measurement. For the leakage inductance in high phase current, which is not considered in two-dimensional (2-D) FEA, the measured value is a little lower than that of FEA value. When the phase current is 280 A_{rms}, the maximum discrepancy between the analysis and the measurement is 37.4 N·m, about 8.9%, which seems reasonable.

The relationship between i_d and back-EMF is shown in Fig. 25, which plotted the effect of different i_d excitations on voltage. When the speed becomes higher, the filed-weakening effect of i_d is obvious. The maximum error between the measurement and FEA is 20 V, while the maximum error between 3-D FEA results and experiment is 10V. Because the simulation results adopt 2-D model, which ignores the flux leakage at the end of the winding. On the other hand, under the low speed conditions, the induced back-EMF is small. The 3D FEA results are closer to the experimental values when considering the accuracy of the model.

The performance boundaries of the vehicle can be determined by the power and efficiency characteristics, so they need to be evaluated conservatively. The maximum power envelope within 6000 r/min at the limit of 280 A_{rms} of phase

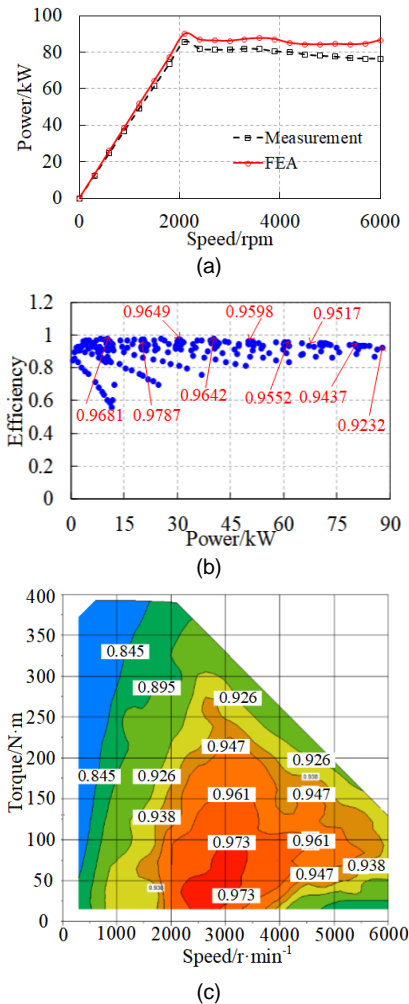


Fig. 26. Power and efficiency. (a) Power (at 300 Arms of phase current and 420 V of line-to-line voltage). (b) Efficiency of different power under WLTP. (c) Measured efficiency map under WLTP.

current and 420 V DC-bus voltage is shown in Fig. 26 (a). The output power is 80.56 kW of measurement and 84.59 kW by FEA at 280 A_{rms} of phase current, 3000 r/min. It can be seen that, under the flux-weakening condition at high speed, the value of measurement and FEA appears a great deviation, about 9.57% because of the leakage flux at the interpolar and magnetic saturation.

Table V is the specifications of the vehicle. Under Worldwide Harmonized Light Vehicles Test Procedure (WLTP), the average efficiency for different powers is 95.66% which is shown in Fig. 26 (b). Fig. 26 (c) is the efficiency map of the proposed motor under the given DC link voltage of 420 V which covers the entire operable points. It can be seen that when the motor operates at rated speed, 97.3% is achievable for the maximum efficiency.

VI. CONCLUSION

This paper has proposed and investigated a 16-pole-72-slot motor with high saliency ratio rotor for E-REVs application. Electromagnetic properties are analyzed to characterize the motor with the proposed rotor. By comparing the

electromagnetic performance of three motors with different rotors. The following conclusions are drawn:

1) Compared with spoke-type flux-concentrating motor, the rotor flux leakage is further reduced with improving saliency ratio. The maximum saliency ratio is increased by 30.2%. The reluctance torque is fully utilized when the motor runs under high current conditions

2) By comparing with a spoke-type motor, when the magnet volume are the same, the peak torque and power of the proposed topology are increased by 17.9% and 4.1%.

3) The FEA results are verified through experiments in detail, which shows that the experimental data are in good agreement with the FEA results. These results show that the motor with the proposed rotor can be of interest in EREVs and EVs applications, because of the flux-concentrating capability and high saliency ratio.

4) To further demonstrate the advantages of this proposed rotor topology, a motor with the novel flux-concentrating IPM rotor will be developed and fabricated for EVs. The maximum speed of traction system is expected to be 24000 r/min and the peak torque is expected to be 500 N·m. The performance will be compared with a conventional V-type IPM machine with the segmented rotor with carbon fiber protection of Tesla Model 3.

REFERENCES

- [1] C. Lv, X. Hu, A. Sangiovanni-Vincentelli, Y. Li, C. M. Martinez, and D. Cao, "Driving-style-based co-design optimization of an automated electric vehicle: A cyber-physical system approach," *IEEE Trans. Ind. Electron.*, vol. 66, no. 4, pp. 2965–2975, Apr. 2019.
- [2] A. Y. S. Lam, Y.-W. Leung, and X. Chu, "Electric vehicle charging station placement: Formulation, complexity, and solutions," *IEEE Trans. Smart Grid*, vol. 5, no. 6, pp. 2846–2856, Nov. 2014.
- [3] A. Poullikkas, "Sustainable options for electric vehicle technologies," *Renewable Sustain. Energy Rev.*, vol. 41, pp. 1277–1287, May. 2015.
- [4] S. Chopra and P. Bauer, "Driving range extension of EV with on-road contactless power transfer—A case study," *IEEE Trans. Ind. Electron.*, vol. 60, no. 1, pp. 329–338, Jan. 2013.
- [5] B.-C. Chen, Y.-Y. Wu, and H.-C. Tsai, "Design and analysis of power management strategy for range extended electric vehicle using dynamic programming," *Appl. Energy*, vol. 113, no. 1, pp. 1764–1774, 2014.
- [6] Philip Karl-Heinz Dost, Philipp Spichartz, and Constantinos Sourkounis, "Charging behavior of users utilizing battery electric vehicles and extended range electric vehicles within the scope of a field test," *IEEE Trans. Ind. Appl.*, vol. 54, no. 1, pp. 580–590, Jan. 2018.
- [7] Woong Lee, Haeseong Jeoung, Dohyun Park, and Namwook Kim, "An adaptive concept of pmp-based control for saving operating costs of extended-range electric vehicles," *IEEE Trans. Veh. Technol.*, vol. 68, no. 12, pp. 11505–11512, Dec. 2019.
- [8] K. Vatanparvar, S. Faezi, I. Burago, M. Levorato, and M. A. Al Faruque, "Extended range electric vehicle with driving behavior estimation in energy management," *IEEE Trans. Smart Grid*, vol. 10, no. 3, pp. 2959–2968, May 2019.
- [9] Ying Zhang, Yingjie Zhang, Zhaoyang Ai, Yi Lu Murphey, and Jing Zhang, "Energy optimal control of motor drive system for extending ranges of electric vehicles," *IEEE Trans. Ind. Electron.*, vol. 68, no. 8, pp. 1728–1738, Feb. 2021.
- [10] Z. Yi and P. H. Bauer, "Optimal stochastic eco-routing solutions for electric vehicles," *IEEE Trans. Intell. Transp. Syst.*, vol. 19, no. 12, pp. 3807–3817, Dec. 2018.
- [11] G. De Filippis, B. Lenzo, A. Sornioti, P. Gruber, and W. De Nijs, "Energy efficient torque-vectoring control of electric vehicles with multiple drivetrains," *IEEE Trans. Veh. Technol.*, vol. 67, no. 6, pp. 4702–4715, Jun. 2018.
- [12] X. Qi, G. Wu, P. Hao, K. Boriboonsomsin, and M. J. Barth, "Integrated connected eco-driving system for PHEVs with co-

- optimization of vehicle dynamics and powertrain operations,” *IEEE Trans. Intell. Vehicles*, vol. 2, no. 1, pp. 2–13, Mar. 2017.
- [13] W. Sung, J. Shin, and Y.-S. Jeong, “Energy-efficient and robust control for high-performance induction motor drive with an application in electric vehicles,” *IEEE Trans. Veh. Technol.*, vol. 61, no. 8, pp. 3394–3405, Oct. 2012.
 - [14] K. Imai, T. Ashida, Y. Zhang, and S. Minami, “Theoretical performance of ev range extender compared with plugin hybrid,” *J. Asian Electr. Veh.*, vol. 6, no. 2, pp. 1181–1184, 2008.
 - [15] X. Liu, H. Chen, J. Zhao, and A. Belahcen, “Research on the parameters of interior PMSM used for electric vehicles,” *IEEE Trans. Ind. Electron.*, vol. 63, no. 6, pp. 3533–3545, Jun. 2016.
 - [16] Burak Ozpineci. “Annual progress report for the power electronics and electric motors program,” Oak Ridge Nat. Lab., Oak Ridge, TN, USA, ORNL/SPR-2014/532, Nov. 2014.
 - [17] Burak Ozpineci. “Annual progress report for the electric drive technologies program,” Oak Ridge Nat. Lab., Oak Ridge, TN, USA, ORNL/SPR-2015/626, Oct. 2015.
 - [18] Z. Yang, Fei Shang, I. P. Brown, and M. Krishnamurthy, “Comparative study of interior permanent magnet, induction, and switched reluctance motor drives for EV and HEV applications,” *IEEE Trans. Transp. Electr.*, vol. 1, no. 3, pp. 245–254, Oct. 2015.
 - [19] P. B. Reddy, A. M. El-Refaie, K.-K. Huh, J. K. Tangudu, and T. M. Jahns, “Comparison of interior and surface PM machines equipped with fractional-slot concentrated windings for hybrid traction applications,” *IEEE Trans. Energy Convers.*, vol. 27, no. 3, pp. 593–602, Sep. 2012.
 - [20] X. Ge, Z. Q. Zhu, J. Li, and J. Chen, “A spoke-type IPM machine with novel alternate airspace barriers and reduction of unipolar leakage flux by step-staggered rotor,” *IEEE Trans. Ind. Appl.*, vol. 43, no. 6, pp. 1565–1571, Nov. 2007.
 - [21] K. Kamiev, J. Montonen, M. P. Ragavendra, J. Pyrhonen, J. A. Tapia, and M. Niemela, “Design principles of permanent magnet synchronous machines for parallel hybrid or traction applications,” *IEEE Trans. Ind. Electron.*, vol. 60, no. 11, pp. 4881–4890, Nov. 2013.
 - [22] C. J. Ifedi et al., “Fault-tolerant in-wheel motor topologies for high performance electric vehicles,” *IEEE Trans. Ind. Appl.*, vol. 49, no. 3, pp. 1249–1257, May/Jun. 2013.
 - [23] S. P. Nikam, V. Rallabandi, and B. G. Fernandes, “A high-torque-density permanent-magnet free motor for in-wheel electric vehicle application,” *IEEE Trans. Ind. Appl.*, vol. 48, no. 6, pp. 2287–2295, Nov./Dec. 2012.
 - [24] Y. Fan, L. Zhang, J. Huang, and X. Han, “Design, analysis, and sensorless control of a self-decelerating permanent-magnet in-wheel motor,” *IEEE Trans. Ind. Electron.*, vol. 61, no. 10, pp. 5788–5797, Oct. 2014.
 - [25] G. Pellegrino, A. Vagati, P. Guglielmi, and B. Boazzo, “Performance comparison between surface-mounted and interior PM motor drives for electric vehicle application,” *IEEE Trans. Ind. Electron.*, vol. 59, no. 2, pp. 803–811, Feb. 2012.
 - [26] Wenping Chai, Wenliang Zhao, and Byung-il Kwon, “Optimal design of wound field synchronous reluctance machines to improve torque by increasing the saliency ratio,” *IEEE Trans. Magn.*, vol. 53, no. 11, Nov. 2017, Art. no. 8206604.
 - [27] Xue Zhou, Xiaoyong Zhu, Wenye Wu, Zixuan Xiang, Yongfeng Liu, and Li Quan, “Multi-objective optimization design of variable-saliency-ratio PM motor considering driving cycles,” *IEEE Trans. Ind. Electron.*, vol. 68, no. 8, pp. 6516–6526, Aug. 2021.
 - [28] Jing Wang, Weiwei Geng, Qiang Li, Lei Li, and Zhuoran Zhang, “A new flux-concentrating rotor of permanent magnet motor for electric vehicle application,” *IEEE Trans. Ind. Electron.*, doi: 10.1109/TIE.2021.3116558.
 - [29] Ke Sun and Shaopeng Tian, “Multiobjective optimization of IPMSM with FSCW applying rotor notch design for torque performance improvement,” *IEEE Trans. Magn.*, vol. 58, no. 5, Nov. 2012, Art. no. 8104909.
 - [30] X. Sun, Z. Shi, G. Lei, Y. Guo, and J. Zhu, “Multi-objective design optimization of an IPMSM based on multilevel strategy,” *IEEE Trans. Ind. Electron.*, vol. 68, no. 1, pp. 139–148, Jan. 2021.
 - [31] K. Atallah, J. Wang, and D. Howe, “Torque-ripple minimization in modular permanent-magnet brushless machines,” *IEEE Trans. Ind. Appl.*, vol. 39, no. 6, pp. 1689–1695, Nov./Dec. 2003.
 - [32] Qian Chen, Gaohong Xu, Guohai Liu, Wenxiang Zhao, Lu Liu, and Zhipeng Lin, “Torque ripple reduction in five-phase IPM motors by lowering interactional MMF,” *IEEE Trans. Ind. Electron.*, vol. 65, no. 11, pp. 8520–8531, Sep. 2018.



Jing Wang received the B.E. degree in electrical engineering from the Hebei Agricultural University, Baoding, China, in 2018. She is currently working toward the Ph.D. degree in electromagnetic design of electrical machines with Nanjing University of Science and Technology (NJUST), Nanjing, China.

Her research interests mainly include PM motor for EV applications, fluid field and electromagnetic analysis, multidomain



Weiwei Geng received the B.S. degree in electrical engineering from Nanjing Agricultural University (NJAU), Nanjing, China, in 2012. He received the M.S. and Ph.D. degrees in electrical engineering from Nanjing University of Aeronautics and Astronautics (NUAA), Nanjing, China, in 2014 and 2018, respectively.

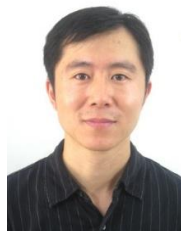
He is now with the Department of Electrical Engineering, Nanjing University of Science and Technology (NJUST). He has published more

than 30 technical papers in journals and conference proceedings. He has 25 issued/published invention patents. His main research interests include PM machines and control, electric drive for electric vehicles and hybrid propulsion.



Jian Guo received his Ph.D. and B.S. degrees in control theory and control engineering from Nanjing University of Science and Technology, China, in 2002 and 1997, respectively. Since 2002, he has been with School of Automation, Nanjing University of Science and Technology, and was promoted to a professor in 2013.

His research interests include intelligent navigation and control, motion control and robot system.



Lei Li received the B.S. degree in electrical technology from Shandong University of Science and Technology, Jinan, China, and the Ph.D. degree in power electronics and power drive from Nanjing University of Aeronautics and Astronautics, Nanjing, China, in 1997 and 2004, respectively.

In 2005, he joined the Faculty of Electrical Engineering, School of Automation, Nanjing University of Science and Technology. His main research interests include switching

mode power supply, multilevel converters and control technique.



Zhuoran Zhang received the B.S. degree in measurement engineering and the M.S. and Ph.D. degrees in electrical engineering from the Nanjing University of Aeronautics and Astronautics (NUAA), Nanjing, China, in 2000, 2003, and 2009, respectively. Since 2003, he has been a Faculty Member with the Department of Electrical Engineering, NUAA, where he is currently a Full Professor and Vice Director of Jiangsu Provincial Key Laboratory of New Energy

Generation and Power Conversion. From February 2012 to June 2013, he was a Visiting Professor with Wisconsin Electric Machines and Power Electronics Consortium (WEMPEC), University of Wisconsin–Madison, Madison, WI, USA. From 2016 to 2017, he worked with Commercial Aircraft Corporation of China, Ltd. (COMAC), Shanghai, China, and was appointed as Deputy Director of electrical system designers of C919 civil jet aircraft.

His research interests include design and control of permanent magnet machines, hybrid excitation electric machines, and doubly salient electric machines for aircraft power, electric vehicles and renewable energy generation. He has authored or coauthored over 170 technical papers and two books, and is the holder of 36 issued patents in these areas.